Infrared spectroscopy of free-floating planet candidates in Upper Scorpius and Ophiuchus

H. Bouy, M. Tamura, D. Barrado, K. Motohara, N. Castro Rodríguez, N. Miret-Roig, M. Konishi, S. Koyama, H. Takahashi, N. Huélamo, et al.

A&A 664, A111 (2022)
https://doi.org/10.1051/0004-6361/202243850

Astronomy & Astrophysics

Infrared spectroscopy of free-floating planet candidates in Upper Scorpius and Ophiuchus*

H. Bouy[1], M. Tamura[2,3], D. Barrado[4], K. Motohara[3], N. Castro Rodríguez[5], N. Miret-Roig[1,6], M. Konishi[2], S. Koyama[7], H. Takahashi[8], N. Huélamo[4], E. Bertin[9], J. Olivares[10], L. M. Sarro[10], A. Berihuete[11], J.-C. Cuillandre[12], P. A. B. Galli[13], Y. Yoshii[7,14], and T. Miyata[7]

[1] Laboratoire d'astrophysique de Bordeaux, Univ. Bordeaux, CNRS, B18N, Allée Geoffroy Saint-Hilaire, 33615 Pessac, France
e-mail: herve.bouy@u-bordeaux.fr
[2] Department of Astronomy, Graduate School of Science, The University of Tokyo, Tokyo, Japan
[3] National Astronomical Observatory of Japan, Tokyo, Japan
[4] Centro de Astrobiología (CSIC-INTA), Depto. de Astrofísica, ESAC Campus, Camino Bajo del Castillo s/n, 28692 Villanueva de la Cañada, Madrid, Spain
[5] Grantecan S. A., Centro de Astrofísica de La Palma, Cuesta de San José, 38712 Breña Baja La Palma, Spain
[6] University of Vienna, Department of Astrophysics, Türkenschanzstraße 17, 1180 Wien, Austria
[7] Institute of Astronomy, Faculty of Science, the University of Tokyo, Osawa 2-21-1, Miaka, Tokyo 181-0015, Japan
[8] Kiso Observatory, Institute of Astronomy, Faculty of Science, the University of Tokyo, Mitake 10762-30, Kiso-machi, Kiso-gun, Nagano 397-0101, Japan
[9] Canada – France – Hawaii Telescope Corporation, 65-1238 Mamalahoa Highway, Kamuela, HI 96743, USA
[10] Depto. de Inteligencia Artificial, UNED, Juan del Rosal, 16, 28040 Madrid, Spain
[11] Depto. Estadística e Investigación Operativa. Universidad de Cádiz, Avda. República Saharaui s/n, 11510 Puerto Real, Cádiz, Spain
[12] AIM, CEA, CNRS, Université Paris-Saclay, Université de Paris, 91191 Gif-sur-Yvette, France
[13] Núcleo de Astrofísica Teórica, Universidade Cidade de São Paulo, R. Galvão Bueno 868, Liberdade, 01506-000 São Paulo, SP, Brazil
[14] Steward Observatory, University of Arizona, 933 North Cherry Avenue, Rm. N204, Tucson, AZ 85721-0065, USA

Received 22 April 2022 / Accepted 2 June 2022

ABSTRACT

Context. A rich population of low-mass brown dwarfs and isolated planetary mass objects has been reported in the Upper Scorpius and Ophiuchus star-forming complex.
Aims. We investigate the membership, nature, and properties of 17 of these isolated planetary mass candidates using low-resolution near-infrared spectra.
Methods. We investigated the membership by looking for evidence of their youth using four diagnostics: the slope of the continuum between the J and Ks band, the $H_{\rm cont}$, and the TLI-g gravity-sensitive indices. In addition, we compared the spectra to young and field (old) M and L-dwarf standards.
Results. All the targets but one are confirmed as young ultracool objects, with spectral types between L0 and L6 and masses in the range 0.004–0.013 $M_{\odot}$, according to evolutionary models. The status of the last target is unclear at this point.
Conclusions. Only one possible contaminant has been identified among the 17 targets, suggesting that the contamination level of the original sample must be low ($\lesssim$6%).

Key words. brown dwarfs – stars: late-type – stars: pre-main sequence – planets and satellites: formation

1. Introduction

Free-floating planets are planetary-mass objects that do not orbit a star, but roam the galaxy in isolation instead. Apart from micro-lensing detections, only a few tens of directly imaged free-floating planet candidates are known to date (e.g., Tamura et al. 1998; Lucas & Roche 2000; Zapatero Osorio et al. 2000; Luhman et al. 2005; Peña Ramírez et al. 2012; Suárez et al. 2019; Lodieu et al. 2018; Luhman & Hapich 2020, and references therein) and only a small fraction have been confirmed so far. Because of the degeneracy in the mass–luminosity relationship for these ultracool objects, it is indeed impossible to distinguish a low-mass brown dwarf from a planetary mass object when the age and distance are unknown. This deadlock can be overcome by studying free-floating planets members of young associations where the age and distance are precisely known. In the context of the COSMIC-DANCE[1] survey Miret-Roig et al. (2022) obtained deep optical and near-infrared photometry and measured accurate proper motions 5 mag beyond Gaia's limit in the nearby Upper Scorpius OB association (USco) and ρ-Ophiuchus (Oph) molecular clouds. They identified over 3500 members, including between 70 and 170 planetary mass objects, depending on the age assumed.

* Full Table B.4 is only available at the CDS via anonymous ftp to cdsarc.u-strasbg.fr (130.79.128.5) or via http://cdsarc.u-strasbg.fr/viz-bin/cat/J/A+A/664/A111

[1] project-dance.com

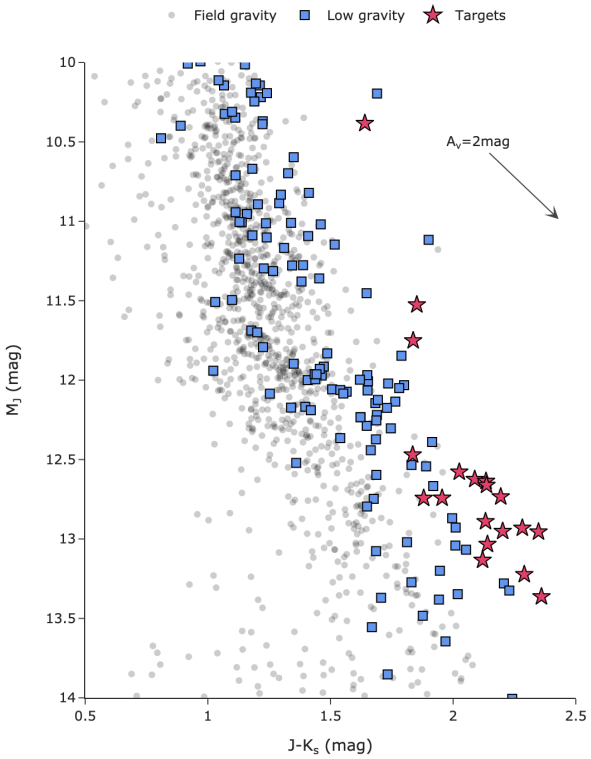

Fig. 1. $(M_J, J-Ks)$ colour–magnitude diagram of our targets (red stars), with low-gravity (blue squares), and field gravity (grey dots) ultracool dwarfs from the literature (Burgasser 2014, and references therein). An arrow represents a $A_V = 2$ mag extinction vector.

This large number of planetary mass object candidates in a young association has important implications for the theories and models of star, brown dwarf, and planet formation. In order to confirm this important discovery, we performed follow-up spectroscopic observations of 18 free-floating planet candidates to confirm their nature and membership to the association and validate Miret-Roig et al. (2022) analysis. In the following, we describe the observations and the processing of the data obtained at the Grantecan and Subaru telescopes. We discuss the membership to the association by looking for spectral features characteristic of young ultracool objects. Finally, we estimate the spectral types of the objects and derive effective temperature and mass estimates, as well as a contamination rate in Miret-Roig et al. (2022) sample.

2. Observations

2.1. Targets

We selected 18 targets within Miret-Roig et al. (2022) sample, after discarding objects already observed spectroscopically in the literature (e.g., Lodieu et al. 2018; Luhman & Esplin 2022). A total of 18 objects were randomly selected in the range between $17.3 < J < 19.2$ mag, corresponding to masses between $7 \lesssim M \lesssim 10\,M_{\rm Jup}$ and effective temperatures between $1500 \lesssim M \lesssim 1900$ K, according to Baraffe et al. (2002) evolutionary models for an age of 5 Myr and a distance of 145 pc. One brighter target (DANCe J16064553−2121595 = 3355, $J = 16.19$ mag) was added during the course of the observations as clouds were degrading the sensitivity and preventing us from observing our original targets. Figure 1 shows a $(M_J, J-Ks)$ color-magnitude diagram of the sample and Fig. 2 shows the location of the targets

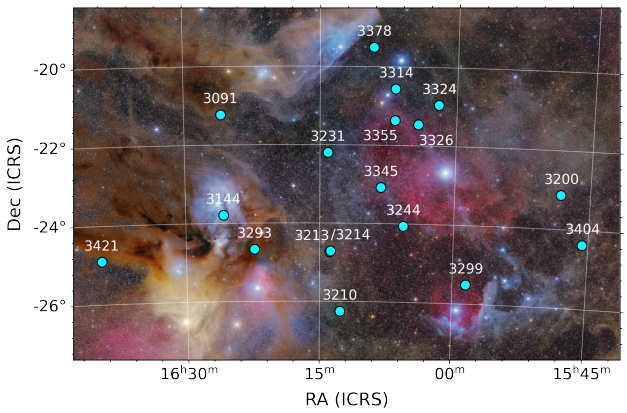

Fig. 2. Position of our targets in Upper Scorpius and Ophiuchus. Background photograph credit: Mario Cogo (galaxlux.com).

in Upper Scorpius and Ophiuchus. Two sources (3213 and 3214) are separated by only 120″.

2.2. SWIMS at Subaru

A total of six objects were observed with the Simultaneous-color Wide-field Infrared Multi-object Spectrograph (SWIMS, Motohara et al. 2014, 2016; Konishi et al. 2018, 2020) mounted on the Subaru Telescope in May 2021 (Program S21A-047, PI: M. Tamura). SWIMS was used in long-slit mode with its simultaneous zJ ($700 < R < 1200$) and HK ($600 < R < 1000$) grisms. The 300 s individual exposures were acquired following a standard ABBA procedure to efficiently remove the sky emission. The seeing was generally very good (between 0.″3 and 0.″6) but clouds were hindering the observations at times. A slit of 0.″5 or 0.″8 was used depending on the seeing. Table 1 gives the list of targets observed with SWIMS and the corresponding number of exposures and individual exposure times. Three B stars of the Upper Scorpius associations were observed (HIP81145, HIP82133 and HIP78702) to be used as telluric standards.

The raw data were processed following standard procedures for infrared spectroscopy using a combination of custom made Python code using the *astropy* and *specutils* libraries (Astropy Collaboration 2018; Earl et al. 2022) and IRAF/PyRAF's *apall* package for the spectra extraction and telluric correction. The closest-in-time B stars spectrum was used to remove the telluric contamination in each of our targets spectra. Because the B stars belong to Upper Scorpius as well, the typical airmass differences with the target were less than 0.2 ∼ 0.3.

2.3. EMIR at GTC

A total of 13 objects were observed with Espectrógrafo Multiobjeto Infra-Rojo (EMIR, Garzón et al. 2014) mounted on the Grantecan telescope (Program GTC2-21A, PI: D. Barrado) in May 2021. EMIR was used in long-slit mode with its HK grism and a slit of 1.″2 chosen to match the ambient seeing during the observations, and leading to an effective resolution of $R \sim 500$. The weather was mostly clear during the observations. Table 1 gives the list of targets observed with EMIR and the corresponding number of exposures and exposure times. The 200 s individual exposures were acquired following a standard ABBA procedure to efficiently remove the sky emission.

The data were reduced using *RedEmIR*, a new GTC pipeline written in Python; *RedEmIR* eliminates the contribution of the

Table 1. Targets observed.

Name	ID [(a)]	RA (J2000)	Dec (J2000)	A_V max. (mag)	i (mag)	z (mag)	y (mag)	J (mag)	H (mag)	Ks (mag)	Exp. time NDIT×DIT s
SWIMS											
DANCe J16135217−2443562	3213	16:13:52.17	−24:43:56.2	0.82	23.76 ± 0.13	22.03 ± 0.05	21.52 ± 0.06	18.84 ± 0.06	17.70 ± 0.05	16.70 ± 0.05	40 × 300
DANCe J16134589−2442310	3214	16:13:45.89	−24:42:31.0	0.82	23.72 ± 0.20	22.05 ± 0.06	21.37 ± 0.05	19.17 ± 0.08	17.73 ± 0.05	16.81 ± 0.05	36 × 300
DANCe J16081299−2304316	3345	16:08:12.99	−23:04:31.6	0.52	23.69 ± 0.08	22.01 ± 0.05	22.15 ± 0.08	18.94 ± 0.05	17.80 ± 0.05	16.82 ± 0.05	24 × 300
DANCe J16064553−2121595	3355	16:06:45.53	−21:21:59.5	0.49	21.03 ± 0.05	19.11 ± 0.05	18.40 ± 0.05	16.19 ± 0.05	15.31 ± 0.05	14.55 ± 0.05	8 × 300
DANCe J16091010−1930376	3378	16:09:10.10	−19:30:37.6	0.60	24.09 ± 0.11	22.19 ± 0.05	21.58 ± 0.05	19.03 ± 0.09	17.81 ± 0.05	16.74 ± 0.05	22 × 300
DANCe J15454024−2422072	3404	15:45:40.24	−24:22:07.2	0.74	23.41 ± 0.10	21.99 ± 0.07	···	18.55 ± 0.06	17.55 ± 0.05	16.67 ± 0.05	22 × 300
EMIR											
DANCe J16221885−2440029	3293	16:22:18.85	−24:40:02.9	2.99	22.20 ± 0.05	20.42 ± 0.05	19.70 ± 0.05	17.33 ± 0.05	16.25 ± 0.05	15.48 ± 0.05	16 × 200
DANCe J16064467−2033428	3314	16:06:44.67	−20:33:42.8	0.77	22.29 ± 0.05	20.45 ± 0.05	19.85 ± 0.05	17.56 ± 0.05	16.50 ± 0.05	15.72 ± 0.05	28 × 200
DANCe J16140756−2211524	3231	16:14:07.56	−22:11:52.4	0.63	23.02 ± 0.05	21.09 ± 0.05	20.78 ± 0.05	18.28 ± 0.05	17.28 ± 0.05	16.44 ± 0.05	24 × 200
DANCe J16255679−2113354	3091	16:25:56.79	−21:13:35.4	1.81	23.53 ± 0.11	21.76 ± 0.05	21.19 ± 0.06	18.39 ± 0.08	17.33 ± 0.05	16.36 ± 0.05	28 × 200
DANCe J16123953−2614510	3210	16:12:39.53	−26:14:51.0	0.88	23.05 ± 0.14	···	20.24 ± 0.05	18.43 ± 0.06	17.31 ± 0.05	16.34 ± 0.05	24 × 200
DANCe J16053908−2403330	3244	16:05:39.08	−24:03:33.0	0.36	23.14 ± 0.07	21.40 ± 0.05	20.87 ± 0.07	18.47 ± 0.05	17.33 ± 0.05	16.33 ± 0.05	32 × 200
DANCe J16020000−2057342	3324	16:02:00.00	−20:57:34.2	0.66	23.15 ± 0.05	21.66 ± 0.05	21.11 ± 0.05	18.54 ± 0.05	17.50 ± 0.05	16.35 ± 0.05	32 × 200
DANCe J16393029−2454135	3421	16:39:30.29	−24:54:13.5	0.69	23.36 ± 0.07	21.69 ± 0.06	20.82 ± 0.05	18.55 ± 0.05	17.44 ± 0.05	16.59 ± 0.05	32 × 200
DANCe J16041234−2127472	3326	16:04:12.34	−21:27:47.2	0.52	23.69 ± 0.07	21.91 ± 0.05	21.53 ± 0.05	18.70 ± 0.05	17.43 ± 0.05	16.57 ± 0.05	32 × 200
DANCe J16254583−2347372	3144	16:25:45.83	−23:47:37.2	3.21	23.64 ± 0.14	21.93 ± 0.06	21.42 ± 0.05	18.74 ± 0.05	17.49 ± 0.05	16.46 ± 0.05	46 × 200
DANCe J15481655−2307430	3200	15:48:16.55	−23:07:43.0	0.77	23.65 ± 0.12	···	···	18.76 ± 0.09	17.50 ± 0.05	16.56 ± 0.05	32 × 200
DANCe J15582895−2530319	3299	15:58:28.95	−25:30:31.9	0.36	23.70 ± 0.12	22.01 ± 0.05	21.41 ± 0.06	18.76 ± 0.06	17.40 ± 0.05	16.41 ± 0.05	32 × 200

Notes. A_V max. corresponds to the integrated line-of-sight interstellar reddening to 250 pc in the direction of the source as computed by Green et al. (2019). The near-infrared JHKs photometry comes in the 2MASS system. [(a)]From Miret-Roig et al. (2022).

sky background in the near infrared using the consecutive A–B pairs. The sky-subtracted images are subsequently flat-fielded, calibrated in wavelength and average combined to obtain the final spectrum. The telluric correction is achieved using a customized version of Xtellcor (Vacca et al. 2003) adjusted to the atmospheric conditions of the La Palma observatory (Ramos Almeida et al. 2009). The spectra are then divided by the spectrum of an A0 star spectrum obtained after or before the targets to remove telluric contamination.

3. Evidence of youth

Young ultra-cool dwarfs such as the ones targeted in the present study have not yet contracted into their final configurations and their gravity is significantly lower than their older field counterparts. At the resolution of our spectroscopic observations, gravity will affect mostly four features:

J to Ks continuum slope: A $J - Ks$ color redder than that of field brown dwarfs has been systematically reported for young brown dwarfs (e.g. Kirkpatrick et al. 2008; Delorme et al. 2017a) as well as for some young planets and brown dwarf companions to stars (e.g., Barman et al. 2011; Delorme et al. 2017b, and Fig. 1). The lower gravity leads to more clouds in the upper layers of the atmosphere, which reduce the amount of emergent flux at shorter wavelengths and lead to fainter absolute J-band magnitudes and redder $J - Ks$ colors. Additionally, the lower density (associated with lower gravity) results in reduced collision-induced H_2 and FeH absorption which in turn leads to less suppression of the K-band flux and therefore a redder $J - Ks$ color (Mohanty et al. 2007; Faherty et al. 2013).

Triangular H-band continuum: Only part of the H-band flux is affected by this reduced collision-induced FeH and H_2 absorption, producing an H-band continuum with a characteristic triangular shape (Lucas et al. 2001) which can be quantified and measured using the $H_{\rm cont}$ index proposed by Allers & Liu (2013). It is insensitive to reddening but the presence of dust in the upper layer of the atmosphere can mimic the effect of low-gravity on the H-band shape. For this reason, Allers & Liu (2013) recommends to complement the $H_{\rm cont}$ index with other diagnostics to test the youth of ultracool objects.

Gravity-sensitive absorption lines: Collision-induced pressure broadening depends on both the temperature and gravity (through the density) in the ultracool dwarf atmosphere. For a given effective temperature, an older ultracool dwarf with a higher gravity will therefore have more prominent absorption lines than a younger (lower gravity) counterpart (Martin et al. 1996; Gorlova et al. 2003; Allers & Liu 2013). At the resolution of our observations, the 1.244 and 1.253 μm K I lines are the most gravity sensitive lines detectable in the SWIMS spectra. Unfortunately, the relatively low signal-to-noise ratio (S/N) of our SWIMS spectra in the J-band results in large uncertainties and inconclusive values of the KI_J index of Allers & Liu (2013).

TLI-g gravity sensitive index: Taking advantage of the growing number of near-infrared spectra available in the literature and in various databases, Almendros-Abad et al. (2022) recently used machine learning techniques to define a new gravity sensitive index. Their TLI-g index is designed to separate young objects from older field objects with a performance superior to other indices from the literature. It seems to be particularly less sensitive to the presence of dust in the upper layer of the atmosphere, but it is, however, sensitive to extinction.

In the following, we discuss the $J - Ks$ color, $H_{\rm cont}$ and TLI-g indices of our targets and compare their spectra to young and field M and L-dwarf standards.

3.1. $J - Ks$ colours

Figure 1 shows that all our targets have $J - Ks$ colors redder than older field counterparts from the literature and similar to known young low-gravity ultracool dwarfs. Both the multiplicity and extinction can shift objects in this diagram and mimic the effect of youth. The presence of an unresolved companion can indeed shift the position mostly vertically in a colour–magnitude diagram and by at most 0.75 mag[2]. While we cannot rule out the presence of unresolved companions, Fig. 1 shows that our targets remain redder than most field L-dwarfs even when adding 0.75 mag to their luminosity. Any unresolved pair would therefore be made of individual components redder than the older

[2] For an equal mass binary the individual fluxes are half the combined flux and the individual magnitudes are $2.5 \log_{10}(2) = 0.75$ mag fainter.

field sequence. Extinction is unlikely to have shifted the objects given that the cumulative line-of-sight reddening towards our objects is low in most cases (see Table 1) and still places them on the redder low-gravity sequence even in the worst cases of 3293 and 3144. While it is not a conclusive proof, the very red $J - Ks$ color certainly adds to the list of evidence indicating youth and, hence, membership to USco or Oph.

3.2. Comparison with young and old M and L standards

To further assess the youth of our targets and at the same time derive their spectral type, we performed an empirical comparison with spectra of young and old ultracool objects from the literature. The comparison was made using The SpeX Prism Library Analysis Toolkit (SPLAT, Burgasser & Splat Development Team 2017). A number of spectral libraries of young ultracool dwarfs have been presented in the literature and we chose to use the very-low gravity spectral standards included in SPLAT (see Table B.2 and Burgasser & Splat Development Team 2017). The field-gravity (older) standards chosen for the comparison are presented in Table B.3.

The degeneracy between extinction and spectral type can affect and compromise the comparison (see e.g., Luhman et al. 2017). To partially lift this degeneracy and explore the effect of extinction on the results of our analysis, we performed the comparison after dereddening our spectra by the cumulative extinction in the line of sight of each target up to 250 pc reported in the 3D extinction map of Green et al. (2019). Assuming that all our targets belong to USco, this should represent a worst-case scenario in terms of reddening and provide an estimate of the lower limit on the spectral type. USco is indeed located at approximately 145 pc and Oph at 125 pc, although possibly extending up to ~200 pc (Damiani et al. 2019). The value of 250 pc was therefore chosen to be conservative and be sure to include the entire depth of the clouds associated with these two regions.

SPLAT was first used to scale the instrumental fluxes to physical units using the target H-band photometry reported in Miret-Roig et al. (2022) as reference. The closest match in each of the two libraries of standards is found using a standard χ^2-minimization. Figures A.1–A.3 show the results, with the original spectra on the left and the dereddened spectra on the right. As expected the spectral types obtained using the high-gravity (older) field standards are systematically later than those obtained with the low-gravity (young) standards.

Figures A.1–A.3 show that 3210, 3200, 3314, 3091, 3326, 3214, 3355, 3144, 3299, and 3345 are clearly better matched by a young spectral standard than by an old spectral standard independently of the reddening.

Among the rest of the sample, we can see that 3378 and 3213 have K-band fluxes significantly higher than the best-match field standards which is clearly pointing towards a young age. The best matches for 3244, 3421, 3231 and 3404 are obtained with a young standard but the χ^2 difference is only marginal and inconclusive. 3293 has a marginally better fit with an old standard but the χ^2 difference is only marginal as well. 3324 displays a very peculiar spectral energy distribution that cannot be matched by any of our old or young standards. While we cannot rule out that the peculiar continuum emission is related to variability, we note that 3324 was observed during degraded ambient conditions and the discrepancy is probably due to telluric clouds absorption, as suggested by the discrepancy between the $H - K_s = 1.15$ mag photometry reported by Miret-Roig et al. (2022) and the synthetic $H - K_s = 0.8$ mag computed from the spectral data. This spectrum is therefore considered as dubious and discarded for the rest of the analysis.

3.3. Sharp H-band continuum

As mentioned earlier in this paper, the shape of the H-band continuum varies from a typical triangular shape at young ages to a flatter continuum at more advanced ages as gravity increases. The $H_{\rm cont}$ index defined by Allers & Liu (2013) is commonly used to quantify the sharpness of the H-band continuum and look for evidence of youth.

We measured the $H_{\rm cont}$ index in all our spectra, as well as in the 891 spectra from the SPEX Ultracool dwarfs library with a good level of quality (`QUALITY_FLAG=OK` and `MEDIAN_SNR` ≥ 50) and a resolution of $R \geq 120$. The uncertainty was estimated by simply propagating the standard errors of the means used in the $H_{\rm cont}$ index formula. We derived near-infrared spectral types for each spectrum from the SPEX Ultracool dwarfs library based on the Kirkpatrick et al. (2010) L-dwarf classification scheme and a gravity classification between very-low (`VL-G`), intermediate (`INT-G`) and field (`FLD-G`) gravity using Allers & Liu (2013) classification scheme. Figure 3 shows the results in the form of a violin graph, using the spectral types presented in Sect. 4 for our targets. The index measurement, spectral type, and gravity classification for the 891 spectra are available in electronic form in Table B.4.

Within the relatively large error bars, a number of our targets seem to have an $H_{\rm cont}$ favoring low or intermediate gravity and hence a young age. These include 3210, 3200, 3314, 3091, 3326, 3214, 3355, 3144, 3299, and 3345. Two objects have $H_{\rm cont}$ values more consistent with high-gravity older objects: 3404 and 3293; however, the broad uncertainties also make them consistent with intermediate gravity objects. Objects 3244, 3421, and 3231 have $H_{\rm cont}$ values that are consistent with intermediate or low gravity, while 3378 and 3213 have inconclusive $H_{\rm cont}$ indices compatible within the uncertainties either with high or intermediate gravity objects.

3.4. TLI-g index

The TLI-g index was invented recently by Almendros-Abad et al. (2022) using machine learning techniques to specifically distinguish low and field gravity ultracool objects. We measured the TLI-g index in all our spectra, as well as in the 891 spectra from the SPEX library mentioned in the previous section (see Table B.4). Figure 4 shows the results in the form of a violin graph.

Within the error bars we can see that all our targets have a TLI-g index favoring low or intermediate gravity and hence a young age except in the case of:

- 3144 with a TLI-g index favoring a field gravity and hence an older age;
- 3378 and 3404 have such large uncertainties that the TLI-g index is inconclusive.

Although Almendros-Abad et al. (2022) defined the TLI-g index using a sample of M0–L3 ultracool dwarfs, we can see in Fig. 4 that it seems to work equally well on the L4 and L6 dwarfs of our sample.

3.5. Final youth status

Table 2 gives a summary of the four youth diagnostics as well as the final status for each target. Among the 17 targets, there are 9 that have the four diagnostics indicating a young age, and are

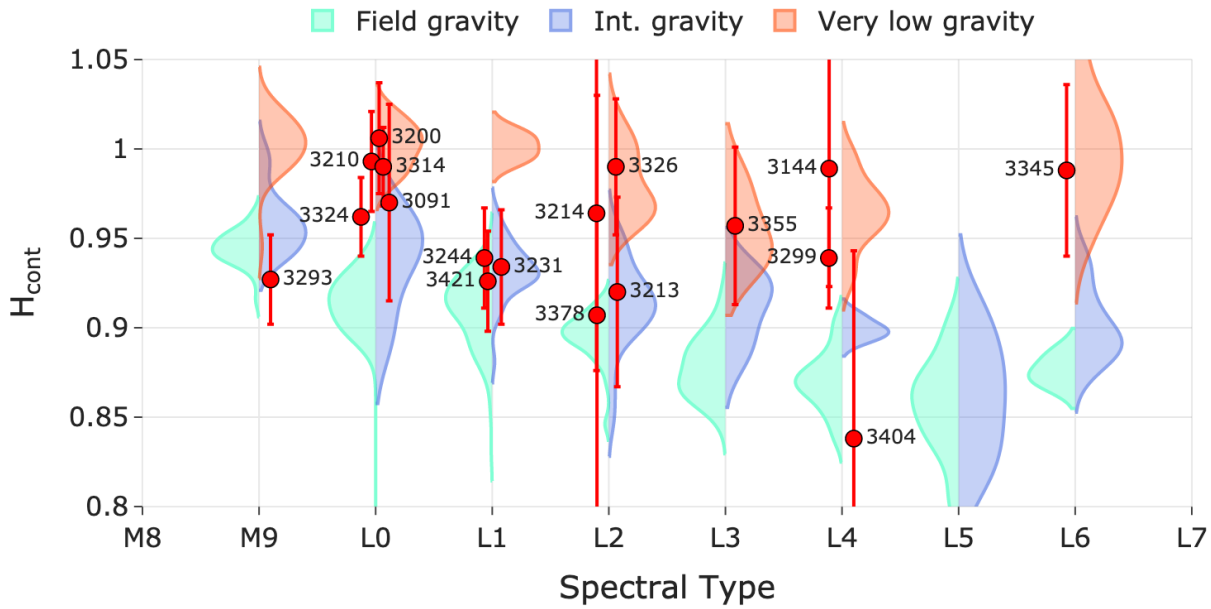

Fig. 3. $H_{\rm cont}$ gravity index from Allers & Liu (2013) for our targets (red dots) over-plotted over a violin graph of the distributions for ultracool dwarfs with very-low gravity (red), intermediate gravity (blue) and field-gravity (cyan) from the SPEX library of ultracool dwarfs. Our targets are shifted randomly horizontally for clarity.

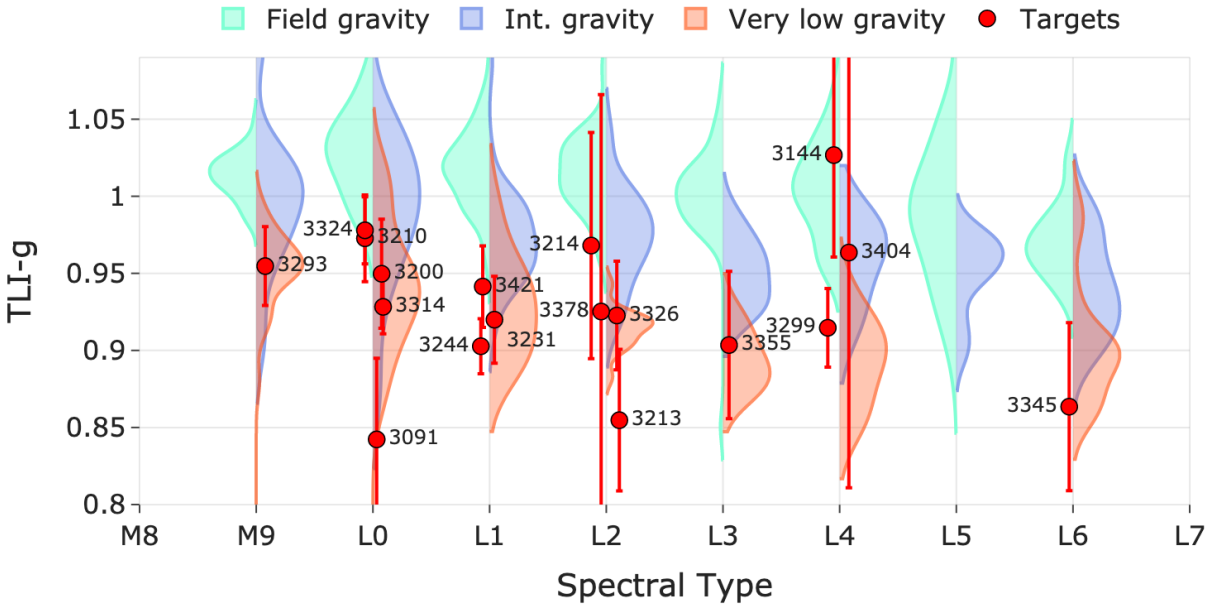

Fig. 4. TLI-g gravity index from Almendros-Abad et al. (2022) for our targets (red dots) over-plotted over a violin graph of the distributions for ultracool dwarfs with very-low gravity (red), intermediate gravity (blue) and field-gravity (cyan) from the SPEX library of ultracool dwarfs. Our targets are shifted randomly horizontally for clarity.

therefore firmly confirmed as young ultracool dwarfs members of the USco and Oph associations. Another 5 have inconclusive $H_{\rm cont}$ indices within the broad uncertainties or an inconclusive comparison with standards – however, all of them have other diagnostics indicating low-gravity and are therefore confirmed as young ultracool dwarfs with a high level of confidence as well.

The remaining cases are discussed here:

– 3144 is classified as young from the $J-Ks$ color, the comparison with spectral standards, and the $H_{\rm cont}$ index, but as old from the TLI-g index. Extinction can affect the TLI-g measurement, but would move the object down in the diagram and make it look younger. Instead, we find that 3144 has a higher TLI-g value. Its value is still consistent with intermediate gravity object within the uncertainties and given that all the other diagnostics favor a young age, we classified 3144 as a young ultracool dwarf as well;
– 3404 is classified as young using two diagnostics and is only classified as possibly old using the $H_{\rm cont}$ index, while the TLI-g index is inconclusive because of the large uncertainties. Given that the large uncertainties on the $H_{\rm cont}$ index make it fully compatible with intermediate and low gravity objects as well, we classified 3404 as young as well;
– 3293 has a marginally better fit with an old standard and has a $H_{\rm cont}$ index clearly favoring a high-gravity older object. But

Table 2. Diagnostics of youth.

ID	$J-Ks$	Comparison with standard	H_{cont}	TLI-g	Young?
3091	Young	Young	Young	Young	Young
3144	Young	Young	Young	Old	Young
3200	Young	Young	Young	Young	Young
3210	Young	Young	Young	Young	Young
3213	Young	Young	?	Young	Young
3214	Young	Young	Young	Young	Young
3231	Young	Young?	Int?	Young	Young
3244	Young	Young?	Int?	Young	Young
3293	Young	Old?	Old?	Young	?
3299	Young	Young	Young	Young	Young
3314	Young	Young	Young	Young	Young
3326	Young	Young	Young	Young	Young
3345	Young	Young	Young	Young	Young
3355	Young	Young	Young	Young	Young
3378	Young	Young	?	?	Young
3404	Young	Young?	Old?	?	Young
3421	Young	Young?	Int?	Young	Young

the $J-Ks$ color and TLI-g index are favoring a young object. The integrated line-of-sight extinction at 250 pc is relatively large ($A_V = 2.99$ mag) and its $J-Ks$ color and TLI-g index might therefore be affected by reddening. With the current data it is difficult to draw any conclusions about the youth of 3293.

In conclusion, 16 of the 17 targets have multiple pieces of evidence to support their youth and one (3293) is inconclusive. In total we therefore firmly confirm the youth of 16 candidates out of 17 as young L-dwarfs members of the USco and Oph associations, or 94%.

4. Spectral types, effective temperature and masses

We then use Figs. A.1–A.3 to estimate the spectral types of the 16 targets with evidence of youth identified in the previous section. With the question of their youth settled, we are left to decide whether extinction affects the spectrum of the targets. By using the integrated line-of-sight extinction towards each target until 250 pc, we can partially break the degeneracy between spectral type and reddening and check the worst-case scenario in which the target eventually lies at the far edge of the association.

Figures A.1–A.3 show that extinction does not affect the result of the comparison for 3091, 3200, 3231, 3244, 3299, 3324, 3326, 3421, and 3345. All indeed have fairly small integrated extinction (see Table 1). The match is significantly better without extinction in the cases of 3213 (L2), 3314 (L0), 3210 (L0), and 3144 (L4), especially in the K-band. Finally, the match is equally good with or without dereddening for 3404 (L3–L4), 3378 (L2–L4), 3355 (L1–L3), 3214 (L2–L4). We note that the difference is always smaller than two subclasses and we adopted the corresponding ranges as final spectral type. These results show that reddening does not affect our target substantially, which is in agreement with the integrated line-of-sight extinction at 250 pc and confirm that they are most likely not reddened background contaminants.

These spectral types are translated into effective temperatures using the empirical relationship for young L-dwarfs reported in Faherty et al. (2016), which in turn are translated into masses using the Saumon & Marley (2008) models for 3, 6, and 10 Myr. Given their location in the Scorpius OB2 complex, most of our targets are expected to belong to Upper Scorpius and have ages in the range of 6–10 Myr. Three of them (3421, 3293, 3144; see Fig. 2) are nevertheless located on top of the $\rho-$Ophiuchus molecular clouds and probably belong to the young (1 ∼ 3 Myr) association. Uncertainties on the spectral types (1 to 2 subclasses) translate into uncertainties of the order of 250 K for the effective temperatures and 0.002 $M_\odot$ for the masses at a given age. Table 3 gives the results and shows that all the candidates seem to have masses in the planetary domain, the least massive having a mass of only 0.004–0.006 $M_\odot$ depending on the age. These objects will cool steadily over time, dissolve in the galactic field population and become field T and Y-dwarfs within the next 50 ∼ 100 Myr, as illustrated in Fig. 5.

Table 3. Adopted spectral types and estimated effective temperatures and masses for the confirmed members.

ID	SpT	T_{eff} (K)	Mass 3 Myr ($M_\odot$)	Mass 6 Myr ($M_\odot$)	Mass 10 Myr ($M_\odot$)
3213	L2	1880	0.007	0.010	0.012
3214	L2–L4	1560–1880	0.005–0.007	0.007–0.010	0.009–0.012
3345	L6	1220	0.003	0.004	0.006
3355	L1–L3	1740–1970	0.006–0.008	0.008–0.011	0.011–0.013
3378	L2–L4	1560–1880	0.005–0.007	0.007–0.010	0.009–0.012
3404	L3–L4	1560–1740	0.005–0.006	0.007–0.008	0.009–0.011
3314	L0	2060	0.009	0.012	0.014
3231	L1	1970	0.008	0.011	0.013
3091	L0	2060	0.009	0.012	0.014
3210	L0	2060	0.009	0.012	0.014
3244	L1	1970	0.008	0.011	0.013
3421	L1	1970	0.008	0.011	0.013
3326	L2	1880	0.007	0.010	0.012
3144	L4	1560	0.005	0.007	0.009
3200	L0	2060	0.009	0.012	0.014
3299	L4	1560	0.005	0.007	0.009

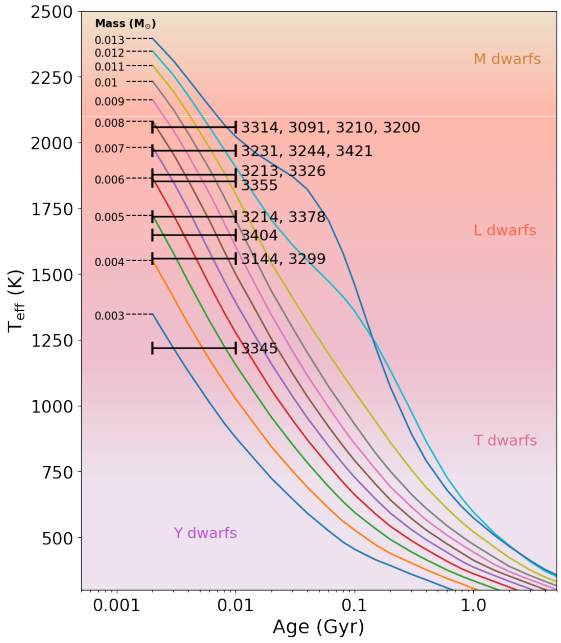

Fig. 5. Effective temperature vs. age between 1 Myr and 15 Gyr according to the Marley et al. (2021) evolutionary models. The targets are represented as well assuming an age between 1 and 10 Myr.

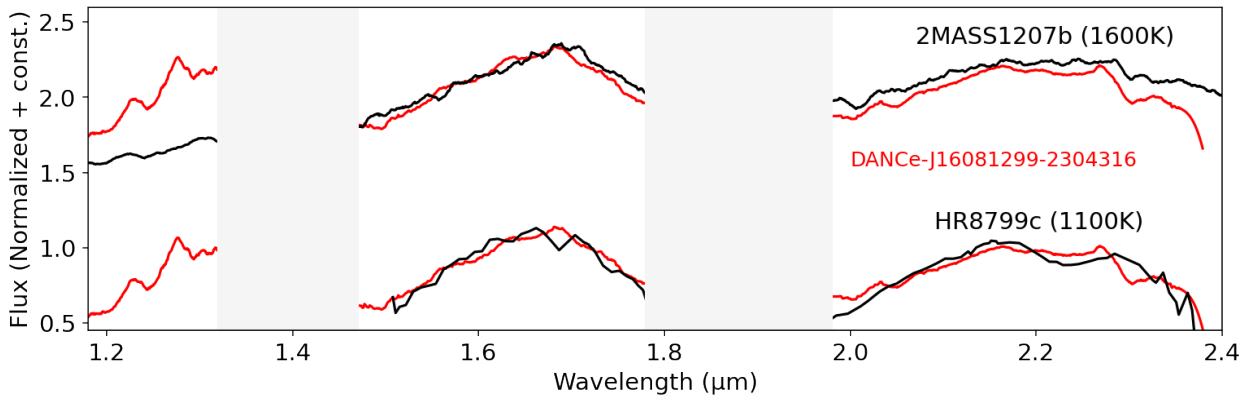

Fig. 6. Smoothed spectrum of DANCe J16081299−2304316 (red) and the planetary mass companion 2MASS J12073346−3932539b and HR8799c from Greenbaum et al. (2018).

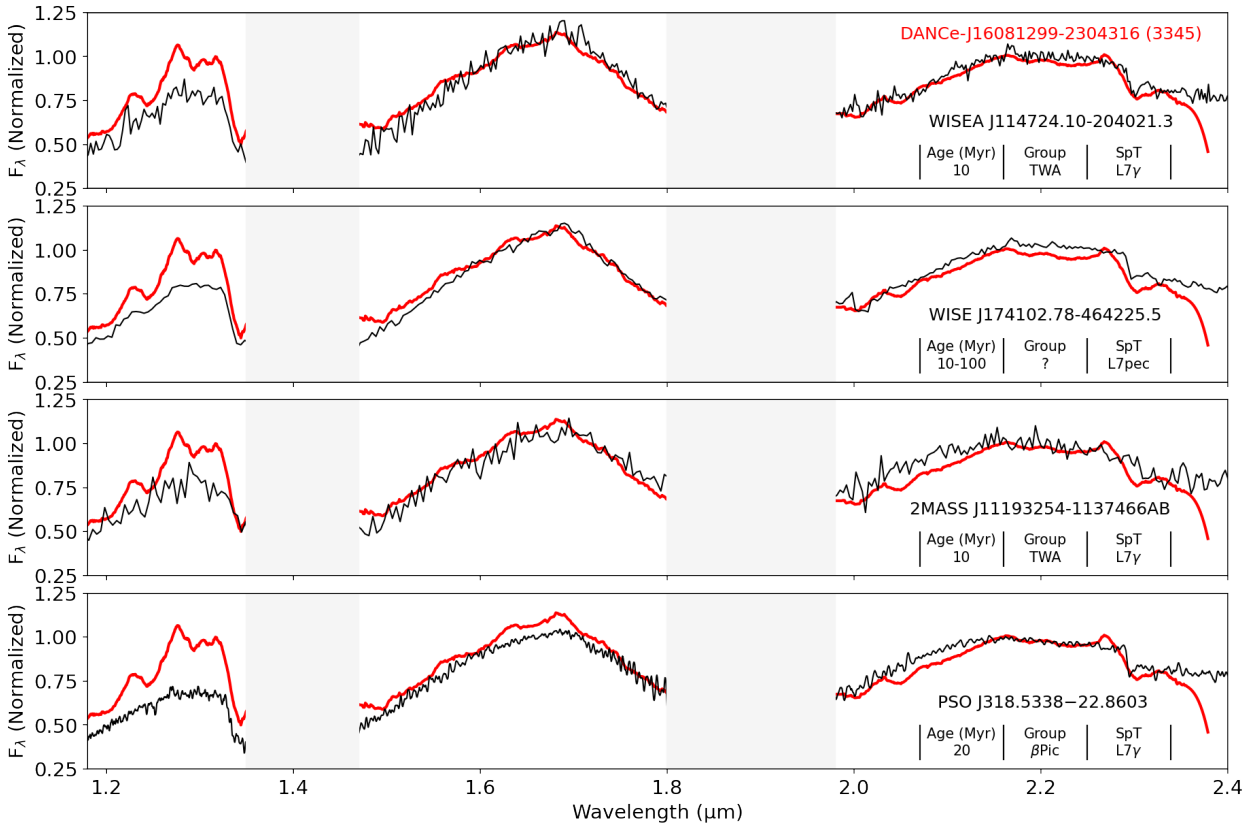

Fig. 7. Smoothed spectrum of DANCe J16081299−2304316 (red) compared to the TW Hydra L7γ free-floating planets WISEA J114724.10−204021.3 (Schneider et al. 2016) and 2MASS J11193254−1137466AB (Kellogg et al. 2016), the young L7pec free-floating planet WISE J174102.78−464225.5 (Schneider et al. 2014), and the β-Pic L7γ free-floating planet PSO J318.5338−22.8603 (Liu et al. 2013).

5. Objects of interest

In the following we discuss a couple of objects of interest: the coolest of our targets and an ultra-wide pair of planetary mass objects.

5.1. The coolest target: DANCe J16081299-2304316 (3345)

In this section and in Figs. 6 and 7, we compare the spectrum of the coolest of our targets, the L6 DANCe J16081299−2304316 (3345) with the spectra of exoplanets and free-floating planets with similar ages and spectral types from the literature.

The *H*-band is generally well matched by all these young exoplanet and free-floating planet spectra, but the overall slope of DANCe J16081299−2304316 is shallower than that of all these objects and the higher *J*-band flux must be due to the slightly earlier spectral type. The 2.3 μm CO overtone is well matched in most free-floating planet spectra but is not as pronounced in the exoplanet spectra. On the other hand the drop observed in DANCe J16081299−2304316 at wavelengths greater than 2.3 μm is observed in HR8799c

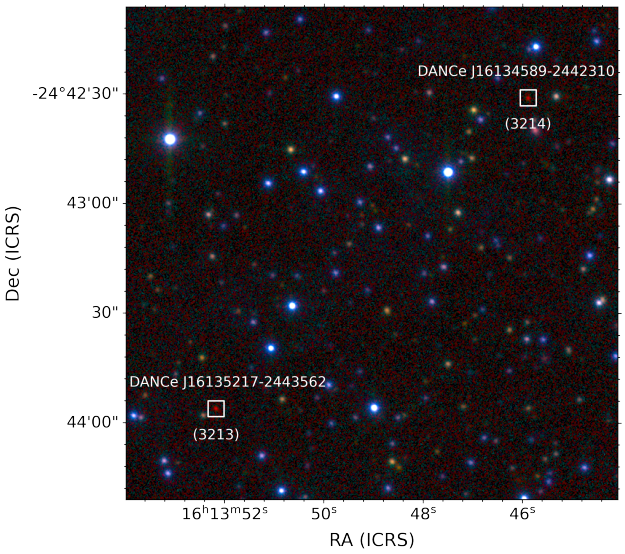

Fig. 8. Three-color image (r, Y, Ks as blue, green, red) of the field around DANCe J16135217−2443562 and DANCe J16134589−2442310. Both are indicated by a square.

spectrum only, making it a good free-floating analog of this directly imaged young gas-giant planet. Overall, the spectrum of DANCe J16081299−2304316 appears most similar to that of HR8799c, and both objects have near-infrared spectral types of L6.

5.2. DANCe J16135217−2443562 and DANCe J16134589−2442310: a possible ultra-wide pair

DANCe J16135217−2443562 (3213) and DANCe J16134589−2442310 (3214) form a wide visual pair with a separation on 120″corresponding to a projected separation of ∼17 400 AU at a distance of 145 pc (as shown in Fig. 8). Such a wide separation for such low-mass objects suggests that it is probably a coincidence rather than a bound physical pair; on the other hand, the very low spatial density of free-floating planets reported in Miret-Roig et al. (2022), of between 0.4 and 1 FFP per square degree, suggests that such a coincidence is highly unlikely and calls for follow-up observations of this intriguing pair. Improved proper motions measurements, along with parallaxes and radial velocities, would help us understand and eventually confirm their common origin. Such a pair could indeed also be a remnant of an extreme case of ultra-wide multiple system such as the ones reported in Taurus (Joncour et al. 2017) or the result of a simultaneous dynamical ejection of two planets in a planetary system.

6. Conclusions

We obtained near-infrared spectra of 18 ultracool candidate members of Upper Scorpius and Ophiuchus discovered by Miret-Roig et al. (2022) using SWIMS at the Subaru telescope and EMIR at the Grantecan telescope. One of the spectra was affected by the poor ambient conditions (clouds) and we discarded it in the analysis.

The spectra allow us to confirm the low gravity and, hence, youth, using four diagnostics: (i) the shape of their H-band continuum measured by the $H_{\rm cont}$ index; (ii) their $J - Ks$ color redder than field counterparts; (iii) by comparison with near-infrared spectra of young L-dwarf standards; (iv) using the TLI-g gravity sensitive index. Among the 17 targets, 16 have multiple pieces of evidence supporting their youth and one (3293) is inconclusive. In total we therefore firmly confirm the youth of 16 candidates out of 17 as young L-dwarfs members of the USco or Ophiuchus association, corresponding to a contamination rate of only $\lesssim$6% and indicating that the methodology devised by Bouy et al. (2013) and Sarro et al. (2014) and used by Miret-Roig et al. (2022) is very reliable.

The spectral types of the targets are estimated via comparisons with young L-dwarf standards, ranging between L0 and L6. Using the Faherty et al. (2016) empirical relationship for young L-dwarfs, we transformed these spectral types into effective temperatures and found that the objects have temperatures in the range between 1220 and 2060 K, corresponding to masses in the range 0.004–0.013 $M_{\odot}$, according to the models of Saumon & Marley (2008) for ages between 3 and 10 Myr, consistent with the Miret-Roig et al. (2022) estimate that is based on the photometry only. Interestingly, even the brightest target (DANCe J16064553−2121595 = 3355) is an early L-dwarf, suggesting that many objects fainter than $M_J \gtrsim 10.5$ mag must indeed have masses in the planetary mass domain.

Acknowledgements. We thank A. Burgasser for his help with SPLAT. We are grateful to M. Bonnefoy, M. Liu, K. Luhman and B. Bowler for sharing spectra of young L-dwarfs and planets. We are grateful to our referee for a thorough review and constructive comments and suggestions. This research has received funding from the European Research Council (ERC) under the European Union's Horizon 2020 research and innovation programme (grant agreement No 682903, P.I. H. Bouy), and from the French State in the framework of the "Investments for the future" Program, IdEx Bordeaux, reference ANR-10-IDEX-03-02. P.A.B.G. acknowledges financial support from São Paulo Research Foundation (FAPESP) under grants 2020/12518-8 and 2021/11778-9. D.B. and N.H. have been partially funded by the Spanish State Research Agency (AEI) Project No. PID2019-107061GB-C61 and MDM-2017-0737 Unidad de Excelencia María de Maeztu – Centro de Astrobiología (CSIC-INTA). Based on observations made with the Gran Telescopio Canarias (GTC), installed in the Spanish Observatorio del Roque de los Muchachos of the Instituto de Astrofísica de Canarias, in the island of La Palma. This work is partly based on data obtained with the instrument EMIR, built by a Consortium led by the Instituto de Astrofísica de Canarias. EMIR was funded by GRANTECAN and the National Plan of Astronomy and Astrophysics of the Spanish Government. Based in part on data collected at Subaru Telescope which is operated by the National Astronomical Observatory of Japan and obtained from the SMOKA, which is operated by the Astronomy Data Center, National Astronomical Observatory of Japan. This research has made use of the VizieR catalogue access tool, CDS, Strasbourg, France. The original description of the VizieR service was published in A&AS, 143, 23. This work made use of GNU Parallel (Tange 2011), astropy (Astropy Collaboration 2013, 2018), Topcat (Taylor 2005), specutils (Earl et al. 2022), matplotlib (Hunter 2007), Plotly (Plotly Technologies Inc. 2015), Numpy (Harris et al. 2020), aplpy (Robitaille & Bressert 2012; Robitaille 2019).

References

Allers, K. N., & Liu, M. C. 2013, ApJ, 772, 79
Almendros-Abad, V., Mužić, K., Moitinho, A., Krone-Martins, A., & Kubiak, K. 2022, A&A, 657, A129
Astropy Collaboration (Robitaille, T. P., et al.) 2013, A&A, 558, A33
Astropy Collaboration (Price-Whelan, A. M., et al.) 2018, AJ, 156, 123
Baraffe, I., Chabrier, G., Allard, F., & Hauschildt, P. H. 2002, A&A, 382, 563
Bardalez Gagliuffi, D. C., Burgasser, A. J., Gelino, C. R., et al. 2014, ApJ, 794, 143
Barman, T. S., Macintosh, B., Konopacky, Q. M., & Marois, C. 2011, ApJ, 735, L39
Bouy, H., Bertin, E., Moraux, E., et al. 2013, A&A, 554, A101
Burgasser, A. J. 2007, ApJ, 659, 655
Burgasser, A. J. 2014, Astron. Soc. India Conf. Ser., 11, 7
Burgasser, A. J., & Splat Development Team 2017, Astron. Soc. India Conf. Ser., 14, 7
Burgasser, A. J., McElwain, M. W., Kirkpatrick, J. D., et al. 2004, AJ, 127, 2856
Burgasser, A. J., Liu, M. C., Ireland, M. J., Cruz, K. L., & Dupuy, T. J. 2008, ApJ, 681, 579
Cruz, K. L., Kirkpatrick, J. D., & Burgasser, A. J. 2009, AJ, 137, 3345

Damiani, F., Prisinzano, L., Pillitteri, I., Micela, G., & Sciortino, S. 2019, A&A, 623, A112
Delorme, P., Dupuy, T., Gagné, J., et al. 2017a, A&A, 602, A82
Delorme, P., Schmidt, T., Bonnefoy, M., et al. 2017b, A&A, 608, A79
Earl, N., Tollerud, E., Jones, C., et al. 2022, https://doi.org/10.5281/zenodo.6207491
Faherty, J. K., Rice, E. L., Cruz, K. L., Mamajek, E. E., & Núñez, A. 2013, AJ, 145, 2
Faherty, J. K., Riedel, A. R., Cruz, K. L., et al. 2016, ApJS, 225, 10
Garzón, F., Castro-Rodríguez, N., Insausti, M., et al. 2014, in Ground-based and Airborne Instrumentation for Astronomy V, eds. S. K. Ramsay, & I. H. Takami, SPIE Conf. Ser., 9147, 91470U
Gizis, J. E. 2002, ApJ, 575, 484
Gorlova, N. I., Meyer, M. R., Rieke, G. H., & Liebert, J. 2003, ApJ, 593, 1074
Green, G. M., Schlafly, E., Zucker, C., Speagle, J. S., & Finkbeiner, D. 2019, ApJ, 887, 93
Greenbaum, A. Z., Pueyo, L., Ruffio, J.-B., et al. 2018, AJ, 155, 226
Harris, C. R., Millman, K. J., van der Walt, S. J., et al. 2020, Nature, 585, 357
Hunter, J. D. 2007, Comput. Sci. Eng., 9, 90
Joncour, I., Duchêne, G., & Moraux, E. 2017, A&A, 599, A14
Kellogg, K., Metchev, S., Gagné, J., & Faherty, J. 2016, ApJ, 821, L15
Kirkpatrick, J. D., Cruz, K. L., Barman, T. S., et al. 2008, ApJ, 689, 1295
Kirkpatrick, J. D., Looper, D. L., Burgasser, A. J., et al. 2010, ApJS, 190, 100
Konishi, M., Motohara, K., Takahashi, H., et al. 2018, in Ground-based and Airborne Instrumentation for Astronomy VII, eds. C. J. Evans, L. Simard, & H. Takami, SPIE Conf. Ser., 10702, 1070226
Konishi, M., Motohara, K., Takahashi, H., et al. 2020, SPIE Conf. Ser., 11447, 114475H
Liu, M. C., Magnier, E. A., Deacon, N. R., et al. 2013, ApJ, 777, L20
Lodieu, N., Zapatero Osorio, M. R., Béjar, V. J. S., & Peña Ramírez, K. 2018, MNRAS, 473, 2020
Lucas, P. W., & Roche, P. F. 2000, MNRAS, 314, 858
Lucas, P. W., Roche, P. F., Allard, F., & Hauschildt, P. H. 2001, MNRAS, 326, 695
Luhman, K. L., & Esplin, T. L. 2022, AJ, 163, 26
Luhman, K. L., & Hapich, C. J. 2020, AJ, 160, 57
Luhman, K. L., Adame, L., D'Alessio, P., et al. 2005, ApJ, 635, L93
Luhman, K. L., Mamajek, E. E., Shukla, S. J., & Loutrel, N. P. 2017, AJ, 153, 46
Marley, M. S., Saumon, D., Visscher, C., et al. 2021, ApJ, 920, 85
Martin, E. L., Rebolo, R., & Zapatero-Osorio, M. R. 1996, ApJ, 469, 706
Miret-Roig, N., Bouy, H., Raymond, S. N., et al. 2022, Nat. Astron., 6, 89
Mohanty, S., Jayawardhana, R., Huélamo, N., & Mamajek, E. 2007, ApJ, 657, 1064
Motohara, K., Konishi, M., Takahashi, H., et al. 2014, in Ground-based and Airborne Instrumentation for Astronomy V, eds. S. K. Ramsay, I. S. McLean, & H. Takami, SPIE Conf. Ser., 9147, 2070
Motohara, K., Konishi, M., Takahashi, H., et al. 2016, in Ground-based and Airborne Instrumentation for Astronomy VI, eds. C. J. Evans, L. Simard, & H. Takami, SPIE Conf. Ser., 9908, 99083U
Peña Ramírez, K., Béjar, V. J. S., Zapatero Osorio, M. R., Petr-Gotzens, M. G., & Martín, E. L. 2012, ApJ, 754, 30
Plotly Technologies Inc. 2015, Collaborative Data Science
Ramos Almeida, C., Pérez García, A. M., & Acosta-Pulido, J. A. 2009, ApJ, 694, 1379
Reid, I. N., Lewitus, E., Allen, P. R., Cruz, K. L., & Burgasser, A. J. 2006, AJ, 132, 891
Robitaille, T. 2019, https://doi.org/10.5281/zenodo.2567476
Robitaille, T., & Bressert, E. 2012, Astrophysics Source Code Library [ascl:1208.017]
Sarro, L. M., Bouy, H., Berihuete, A., et al. 2014, A&A, 563, A45
Saumon, D., & Marley, M. S. 2008, ApJ, 689, 1327
Schneider, A. C., Cushing, M. C., Kirkpatrick, J. D., et al. 2014, AJ, 147, 34
Schneider, A. C., Windsor, J., Cushing, M. C., Kirkpatrick, J. D., & Wright, E. L. 2016, ApJ, 822, L1
Suárez, G., Downes, J. J., Román-Zúñiga, C., et al. 2019, MNRAS, 486, 1718
Tamura, M., Itoh, Y., Oasa, Y., & Nakajima, T. 1998, Science, 282, 1095
Tange, O. 2011, The USENIX Magazine, 36, 42
Taylor, M. B. 2005, in Astronomical Data Analysis Software and Systems XIV, eds. P. Shopbell, M. Britton, & R. Ebert, ASP Conf. Ser., 347, 29
Vacca, W. D., Cushing, M. C., & Rayner, J. T. 2003, PASP, 115, 389
Zapatero Osorio, M. R., Béjar, V. J. S., Martín, E. L., et al. 2000, Science, 290, 103

Appendix A: Figures

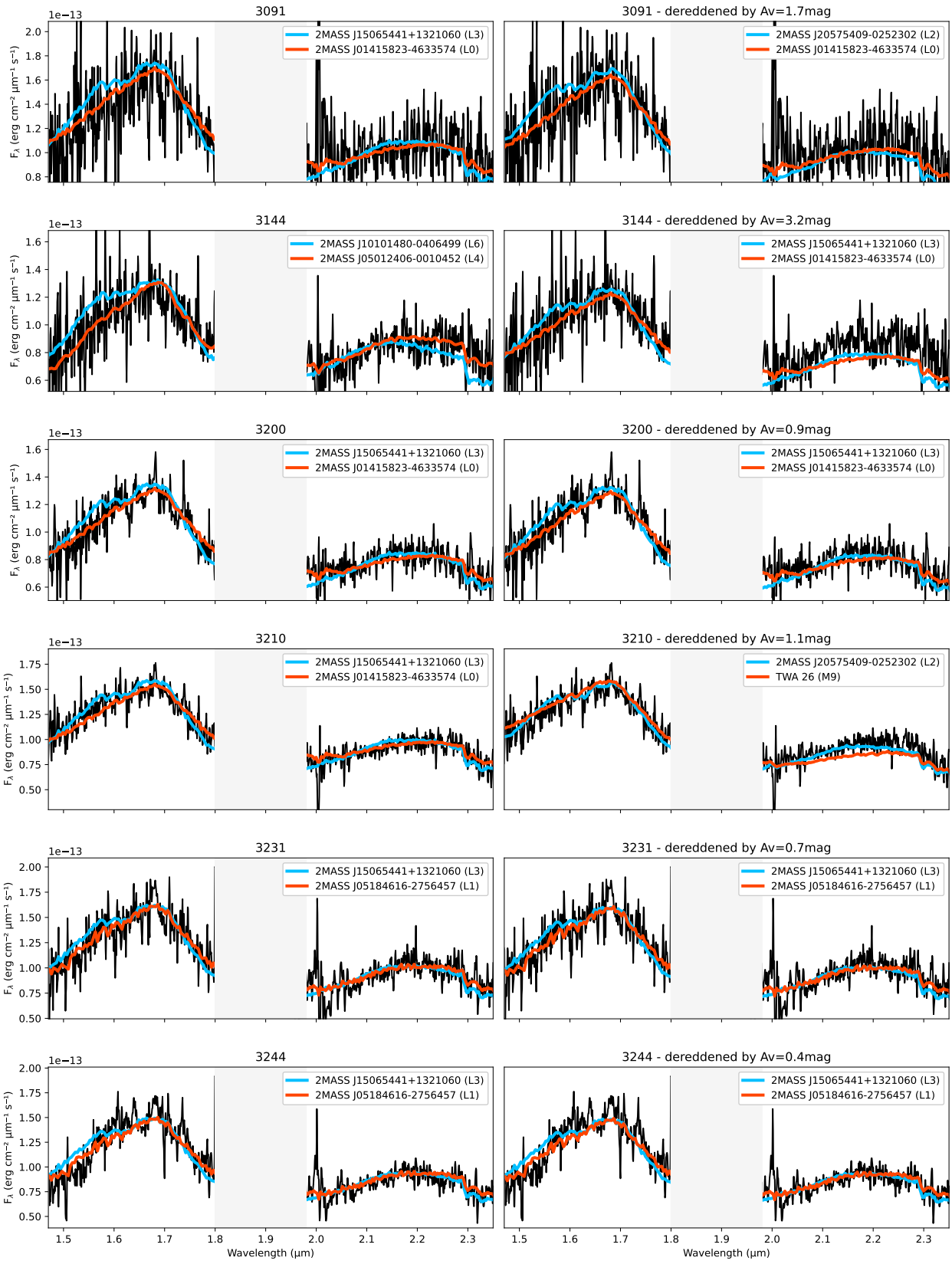

Fig. A.1. Comparison of our targets spectra (black) with very-low gravity standards (red) and field-gravity standards (blue). The left panels show the original spectrum, and the right panels show the spectrum derredened by the cumulative line-of-sight extinction indicated in the plot title and in Table 1.

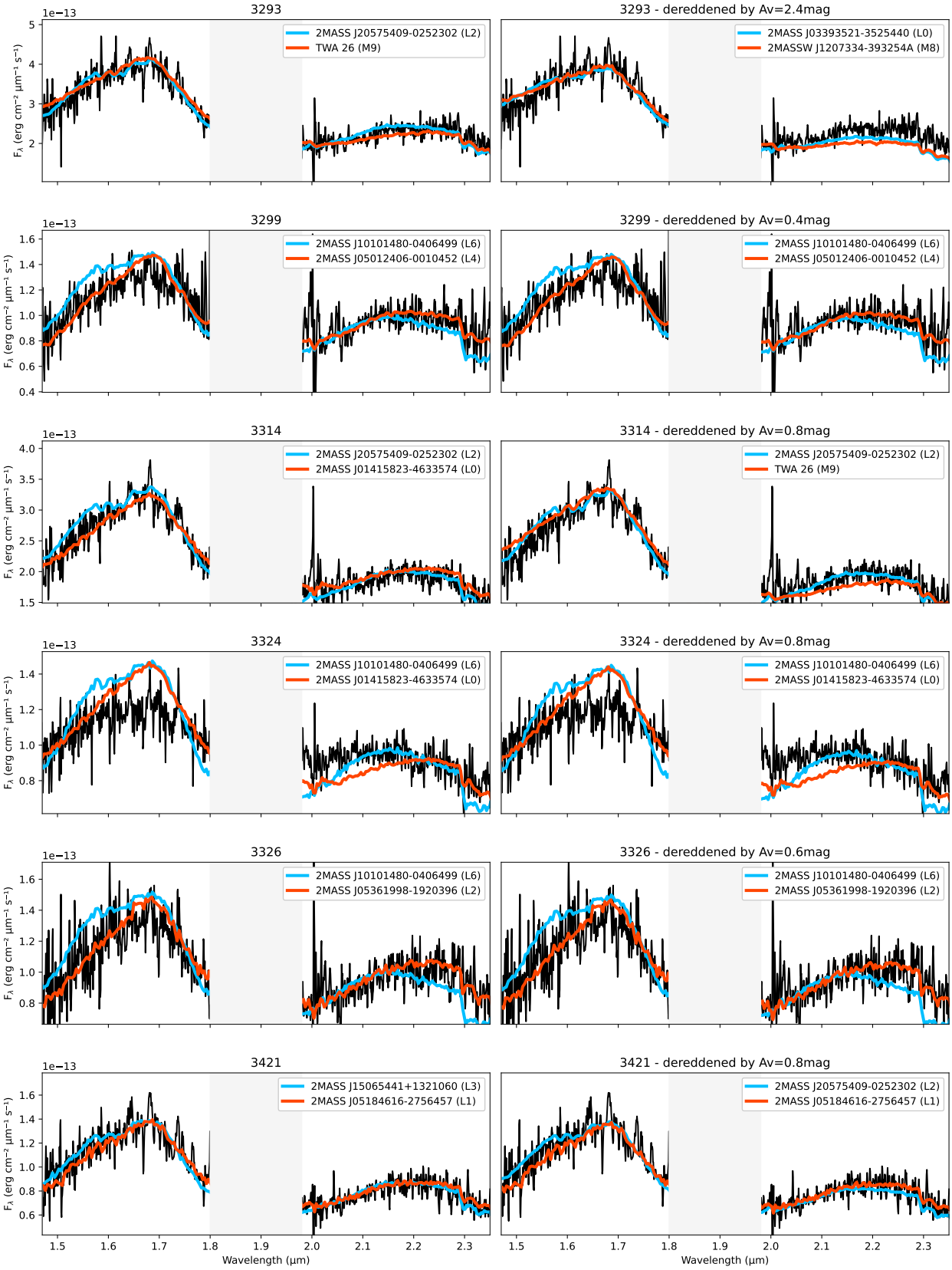

Fig. A.2. Comparison of our targets spectra (black) with very-low gravity standards (red) and field-gravity standards (blue). The left panels show the original spectrum, and the right panels show the spectrum derredened by the cumulative line-of-sight extinction indicated in the plot title and in Table 1.

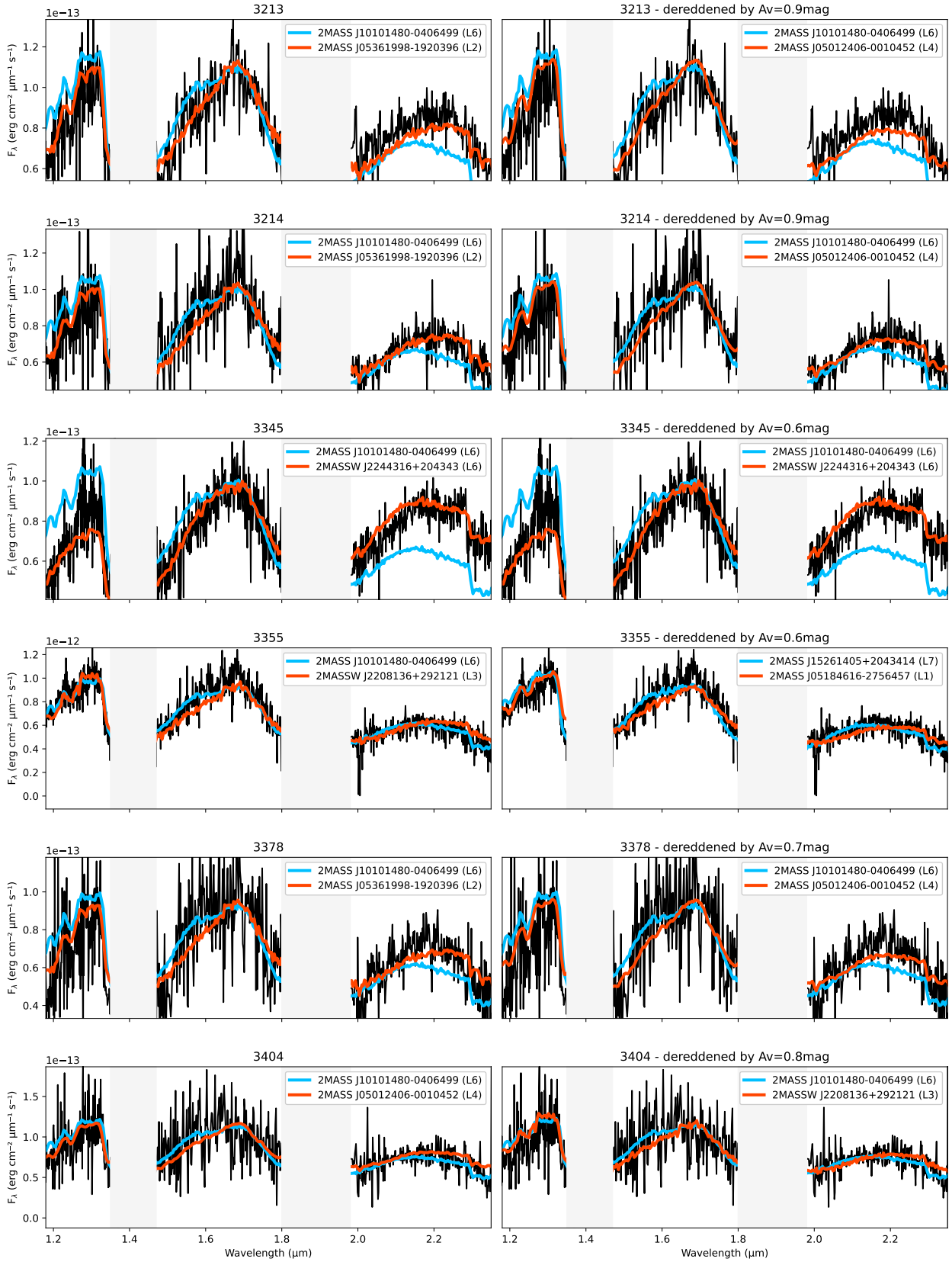

Fig. A.3. Comparison of our targets spectra (black) with very-low gravity standards (red) and field-gravity standards (blue). The left panels show the original spectrum, and the right panels show the spectrum derredened by the cumulative line-of-sight extinction indicated in the plot title and in Table 1.

Appendix B: Tables

Table B.1. Gravity sensitive indices.

Object	H_{cont}	TLI-g
3091	0.97 ± 0.05	0.84 ± 0.05
3144	0.99 ± 0.07	1.03 ± 0.07
3200	1.01 ± 0.03	0.95 ± 0.04
3210	0.99 ± 0.03	0.97 ± 0.03
3213	0.92 ± 0.05	0.85 ± 0.05
3214	0.96 ± 0.09	0.97 ± 0.07
3231	0.93 ± 0.03	0.92 ± 0.03
3244	0.94 ± 0.03	0.90 ± 0.02
3293	0.93 ± 0.03	0.95 ± 0.03
3299	0.94 ± 0.03	0.91 ± 0.03
3314	0.99 ± 0.02	0.93 ± 0.02
3324	0.96 ± 0.02	0.98 ± 0.02
3326	0.99 ± 0.04	0.92 ± 0.04
3345	0.99 ± 0.05	0.86 ± 0.05
3355	0.96 ± 0.04	0.90 ± 0.05
3378	0.91 ± 0.12	0.93 ± 0.14
3404	0.84 ± 0.10	0.96 ± 0.15
3421	0.93 ± 0.03	0.94 ± 0.03

Table B.2. SPEX library of very-low gravity ultracool standards.

Name	RA	Dec	SpT	Ref.
2MASSW J1207334-393254A	181.88959	-39.548443	M8	(1)
TWA 26	174.96304	-31.989279	M9	(1)
2MASS J01415823-4633574	25.492626	-46.565945	L0γ	(2)
2MASS J05184616-2756457	79.692337	-27.946028	L1γ	(3)
2MASS J05361998-1920396	84.083244	-19.344334	L2γ	(3)
2MASSW J2208136+292121	332.05679	29.355972	L3γ	(2)
2MASS J05012406-0010452	75.35025	-0.17922223	L4γ	(2)
2MASSW J2244316+204343	341.13196	20.728695	L7γ	(4)

References. (1) Gizis (2002) ; (2) Cruz et al. (2009) ; (3) Bardalez Gagliuffi et al. (2014) ; (4) Kirkpatrick et al. (2008).

Table B.3. Library of field ultracool standards.

Name	RA (J2000)	Dec (J2000)	SpT	Ref.
VB 10	289.2400917	5.1506056	M8	(2)
LP 944-20	54.89675	-35.4289139	L0	(1)
GJ 1048B	38.9997083	-23.5223611	L1	(1)
2MASSI J2057540-025230	314.4753917	-2.8750722	L2	(2)
2MASSW J1506544+132106	226.7267125	13.3516889	L3	(3)
2MASSW J0036159+182110	9.0674	18.3529083	L4	(1)
SDSSp J144600.60+002452.0	221.5025833	0.4144444	L5	(4)
2MASSI J1010148-040649	152.5616958	-4.1138694	L6	(5)
2MASSI J1526140+204341	231.5585417	20.7281833	L7	(2)

References. (1) Burgasser et al. (2008) ; (2) Burgasser et al. (2004) ; (3) Burgasser (2007) ; (4) Bardalez Gagliuffi et al. (2014) ; (5) Reid et al. (2006).

Table B.4. Gravity sensitive indices measured in 891 spectra of the SPEX library.

Name	RA (J2000)	Dec (J2000)	SpT	SPEX_CLASS	H_{cont}	e_H_{cont}	TLI-g	e_TLI-g
2MASS J0000286-124515	0.11945834	-12.75425	M9.0	FLD-G	0.947	0.003	1.015	0.01
2MASS J00013044+1010146	0.37683335	10.170723	M6.0	VL-G	0.988	0.006	1.009	0.023
LHS 102B	1.1451666	-40.734943	L4.0	FLD-G	0.855	0.002	1.011	0.008
LEHPM 1-162	1.4486667	-21.954889	M8.0	FLD-G	0.963	0.002	0.994	0.009
2MASSI J0006205-172051	1.5854167	-17.347389	L2.0	FLD-G	0.897	0.006	0.998	0.006
SDSS J000632.60+140606.4	1.6358334	14.101778	L1.0	FLD-G	0.931	0.009	0.989	0.017
SDSS J000649.16-085246.3	1.7048334	-8.879528	M8.0	FLD-G	0.921	0.004	1.035	0.008
2MASS J0007078-245804	1.7827917	-24.967834	M8.0	INT-G	0.987	0.003	1.008	0.017
2MASS J00085931+2911521	2.2471251	29.197805	M8.0	INT-G	0.967	0.002	1.013	0.007
2MASS J00100009-2031122	2.500375	-20.520056	M8.0	FLD-G	0.933	0.003	1.049	0.003
2MASSI J0013578-223520	3.4907918	-22.58889	L5.0	FLD-G	0.859	0.01	0.992	0.01
WISE J001450.14-083823.1	3.7089167	-8.6397219	M7.0	FLD-G	0.945	0.008	1.042	0.016
2MASS J00145575-4844171	3.7322917	-48.738083	L3.0	FLD-G	0.883	0.006	1.022	0.013
2MASSW J0015447+351603	3.9364998	35.267387	L2.0	INT-G	0.9	0.003	1.025	0.006
SDSS J001608.44-004302.3	4.0351253	-0.71722221	L3.0	INT-G	0.898	0.008	0.961	0.023
2MASS J00163761+3448368	4.1567087	34.810223	M8.0	FLD-G	0.939	0.004	1.016	0.013

Notes. The entire table is available electronically at the CDS.